



ELSEVIER

Engineering Analysis with Boundary Elements 28 (2004) 345–357

ENGINEERING
ANALYSIS *with*
BOUNDARY
ELEMENTS

www.elsevier.com/locate/enganabound

A fully non-linear model for atomization of high-speed jets

Sam S. Yoon*, Stephen D. Heister

School of Aeronautics and Astronautics, Purdue University, 1614 Shining Armor Lane, West Lafayette, IN 47906, USA

Received 9 November 2002; revised 14 February 2003; accepted 20 February 2003

Abstract

A non-linear model has been developed to assess the time evolution of an axisymmetric liquid jet using a boundary-element method. Vorticity transported from the boundary layer in the orifice passage to the free surface is modeled using a potential ring vortex placed at the orifice exit plane. The vortex strength is uniquely determined from the Kutta condition and information regarding the boundary layer thickness at the orifice exit plane. It is shown that primary breakup can occur even in the absence of the gas phase. Using a secondary stability analysis after Ponstein [Appl. Scientific Res. 8 (1959) 425], the size of the droplets is estimated based on the size of the ring-type structures shed from the periphery of the jet. Computed droplet sizes are in reasonable agreement with experimental data, although turbulence effects obscure some comparisons.

© 2003 Elsevier Ltd. All rights reserved.

Keywords: Atomization; Jet; Vortex-ring

1. Introduction

The atomization of a liquid jet is one of the most fundamental problems of two-phase flow and has received much attention due to the large number of practical applications. Since the formation of droplets is ultimately dictated by a balance of capillary and inertial forces, numerical methods that provide high resolution of these forces perform best in simulating these flows. The capillary force depends on local surface curvature, which is a function of surface shape with dependence on second derivatives of local surface coordinates. Resolving the curvature accurately is of paramount importance in these problems. For these reasons, the Boundary-Element Method (BEM) is uniquely suited for atomization modeling in that the optimal placement of nodes on the gas/liquid interface provides a mean for maximizing accuracy of surface curvature calculations.

BEM techniques have been applied to a wide variety of free surface/atomization problems including liquid jets [2–10], droplets [11,12] and electrostatic atomization [13,14]. Along with the difficulty in computing surface curvature, the inherent non-linearity of the free-surface condition has been addressed by many researchers. Several

proven techniques available at the present time. In the liquid jets field, high-resolution and high fidelity BEM solutions for low-speed flows are now available and applicable to problems in chemical engineering and inkjet printing.

Despite these advances, the atomization process increases in complexity with increasing jet speed. For this reason, the modeling of high-speed jets which produce small droplets of interest in many application, are still an area requiring significant efforts. Prior research [3,15,16] has indicated the importance of the boundary layer structure at the orifice exit plane in mapping instabilities just downstream of the injection point, as shown in Fig. 1. The present study focuses on this issue via an axisymmetric simulation that properly accounts for the presence of, and vorticity within, this boundary layer. Section 2 provides a description of the model, followed by convergence studies and comparisons with experimental data.

2. Modeling

The model is based on unsteady axisymmetric potential flow of a liquid exiting a round orifice in the absence of a gas-phase medium. A ring vortex is employed to simulate viscous effects associated with vorticity in the boundary layer formed in the orifice passage. Carefully controlled

* Corresponding author. Tel.: +1-765-494-7864; fax: +1-765-494-0307.
E-mail address: yoons@ecn.purdue.edu (S.S. Yoon).

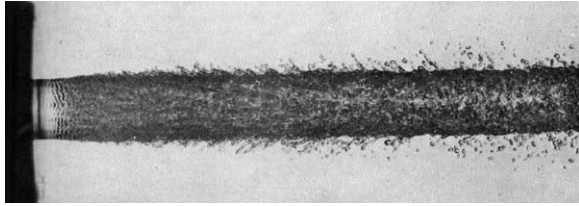


Fig. 1. Typical water jet into air in the atomization regime. Experimental image by Hoyt and Taylor [46]. Printed under the permission of Journal of Fluid Mechanics.

experiments have shown a nearly axisymmetric structure during the early stages of the free-surface instability. Fig. 2 shows a schematic representation of the geometry and nomenclature. The size of the Rankine vortex [17] is defined as R_c , as will be discussed in detail in a later section. A vortex ring of strength Γ_v and overall radius \bar{r} is assumed to lie at the orifice exit plane. A computational domain is represented by a simple cylindrical column of length z_l , and a hemispherical cap is selected to initialize the calculation. Constant nodal spacing, Δs , is employed along this domain, and nodes are added as the jet issues forward from the orifice. Fig. 3 shows the actual flow condition with the current superposition modeling. Because the concentrated vortices at the filament vortex-ring are transported to the free-surface, the jet surface is unstable. We choose the liquid density, ρ , jet average exit velocity, U , and orifice radius, a as characteristic dimensions in the problem.

The formulation of the BEM starts with the integral representation of the solution of Laplace’s equation, $\nabla^2 \phi = 0$, with ϕ being the velocity potential. Following Liggett and Liu [18], the integral form for this relation is given by:

$$\alpha \phi(\vec{r}_i) + \int_{\Omega} \left[\phi \frac{\partial G}{\partial \hat{n}} - qG \right] d\Omega = 0 \tag{1}$$

where $\phi(\vec{r}_i)$ is the value of the potential at a point \vec{r}_i , Ω is the boundary of the 3D domain, and G is the free space Green’s function of Laplace’s equation. If $d\Omega$ is a 3D surface

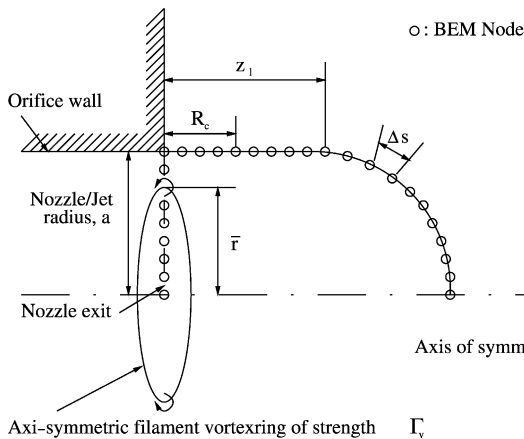


Fig. 2. Schematic of the initial jet geometry indicating computational nodes and the axisymmetric ring vortex at the orifice exit plane.

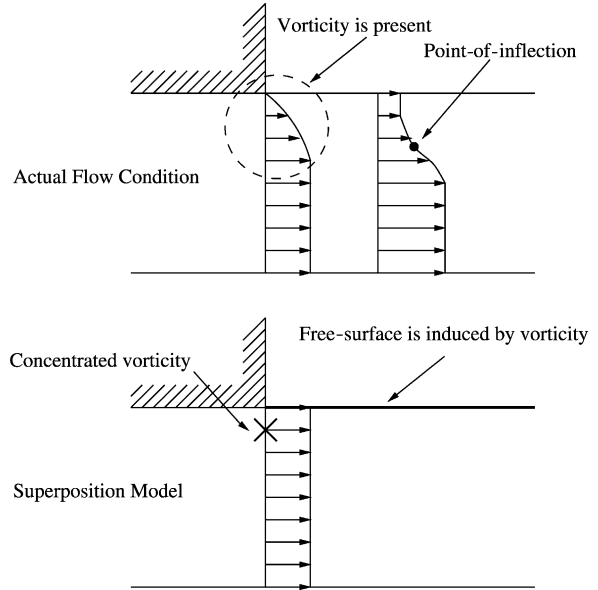


Fig. 3. Comparison of the actual physical flow condition with the superposition model in simulating boundary layer relaxation downstream of the orifice exit plane.

element, ds is a 2D surface with $d\Omega = r d\theta ds$. Then the governing Eq. (1) can be written as:

$$\alpha \phi(\vec{r}_i) + \int_s [\phi D_{\text{kern}} - qS_{\text{kern}}] ds = 0 \tag{2}$$

where the source and doublet kernels are

$$S_{\text{kern}} = \frac{4rK(m)}{\sqrt{\hat{a}}} \tag{3}$$

$$D_{\text{kern}} = -\frac{1}{2\sqrt{\hat{a}}} \left[\hat{n}_r K(m) + \frac{E(m)}{c} [d\hat{n}_r + 2r\hat{n}_z(z - z_i)] \right]$$

and the auxilliary quantities, \hat{a}, c, d are defined:

$$\hat{a} = (r_i + r)^2 + (z - z_i)^2 \quad c = (r - r_i)(z - z_i)^2 \tag{4}$$

$$d = r^2 - r_i^2 - (z - z_i)^2$$

where $m = 4rr_i/\hat{a}$. Here, $K(m)$ and $E(m)$ are the elliptical integral [19] of the first and second kind, respectively, and $\hat{n}_{z,r}$ is the component of the normal vector in z and r direction. We utilize linear elements for the velocity potential,

$$\phi = \phi_j \left(\frac{s_{j+1} - s}{s_{j+1} - s_j} \right) + \phi_{j+1} \left(\frac{s - s_j}{s_{j+1} - s_j} \right) \tag{5}$$

with an analogous form for the normal velocity, $\partial \phi / \partial n = q$. Substitution of Eq. (5) into Eq. (2) yields the following $N_{\text{node}} \times N_{\text{node}}$ matrix:

$$[\alpha I + D][\phi] = [S][q] \tag{6}$$

where α arises from singular contributions to the doublet terms as the integral passes through the base point z_j, r_j .

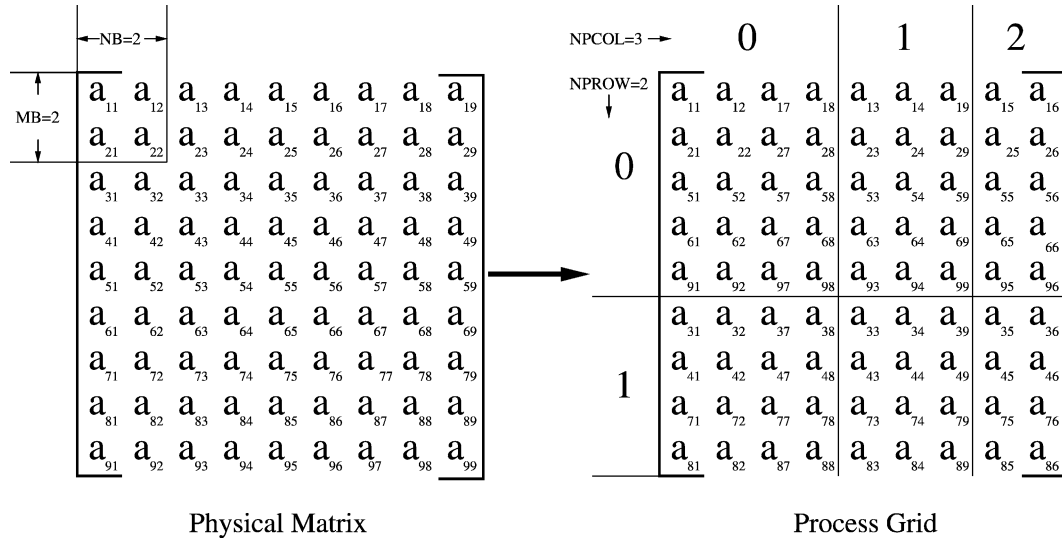


Fig. 4. A 9×9 matrix decomposition with a 2×2 submatrix for a 2×3 process grid.

Because the matrix system can be quite large (i.e. $N_{\text{node}} > 1000$), the matrix inversion step is parallelized to incorporate multiple processors. Since a fourth-order Runge-Kutta time integration scheme is employed, the calculation requires solving the large matrix system four times at every time step. In addition, the size of the computational domain increases in time, which yields a larger matrix system at every time step [20,21]. The Scalable Linear Algebra Package [22] (SCALAPACK) is implemented into the current code as a parallel solver. Under this parallelization, the code can utilize up to N_p number of processor. We have used $N_p = 6$ because little variation is observed for the computational efficiency after $N_p = 6$ with the current 104 node LINUX-Cluster networking system. Here, a tradeoff exists between individual node speed (we use 1.2 GHz Athalon chips) and nodal communication time. Because the nodes are quite fast in performing the required calculations, communication time tends to dominate for $N_p > 6$.

A typical $[A][X] = [B]$ non-parallel solver based on LU-Decomposition is available in Numerical Recipes [23]. When the matrix $[A]$ and vector $[B]$ are given, the matrix $[X]$ can be obtained using the LU-Decomposition. The parallel $[A][X] = [B]$ solver SCALAPACK is also based on the LU-Decomposition algorithm. However, one additional step is required for SCALAPACK: the partition of $[A]$, $[X]$, and $[B]$ into the N_p process grid. Unfortunately, SCALAPACK does not perform the matrix partition autonomously. Thus, we have developed the algorithm for the grid-partition. Considering $N_p = 6$, the physical matrix $[A]$ is transformed into the 2×3 process grid, as shown in Fig. 4. Parameters that define this transformation are $MB \times NB$ for the size of the submatrix, and $NPROW \times NPCOL$ for the number of processors (Fig. 4). The particular parallel solver used for our calculation, called 'pdgesv' [22], can handle the fully dense matrix, $[A]$. If the matrix $[A]$ is tridiagonal, and

'pddtsv' is used for the efficient calculation. In addition, 'pddbsv' solves a general band system $[A][X] = [b]$. It should be noted that the answer $[X]$ is split into 'row' processors. As shown in Fig. 5, we have combined the answer $[X]$ in the (0, 0) processor and broadcast $[X]$ to other processors using the MPI routine.

We have constructed the sample calculation; Laplace equation with the Dirichlet boundary conditions at the side walls and thus $[A]$ is a banded system and 'pdgesv' is used. The sample code can be downloaded at <http://roger.ecn.purdue.edu/~yoons/SCAL.tar.gz>

Flow physics at the smaller length scale can be captured using a finer grid under the parallelization. The length scale of our interest is scaled by the momentum thickness, δ_2 . A complete calculation takes about one to two weeks: this is long enough real time to obtain all the information about the droplet characteristics of our particular interest.

2.1. Superposition

Contributions from the vortex ring can be obtained through the principle of superposition for potential flow.

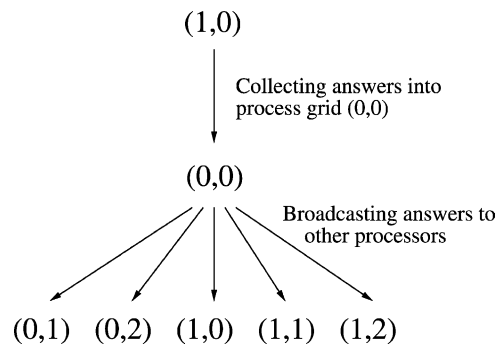


Fig. 5. Passing the solution $[X]$ to all other processors is carried out for all processors to share the information of $[X]$.

Since Laplace's governing equation is linear, we may superpose the bulk potential flow with the flow due to the vortex ring (i.e. ϕ_v or Ψ_v),

$$\phi_t = \phi + \phi_v \quad \Psi_t = \Psi + \Psi_v \quad (7)$$

where ϕ and P_{si} represent the velocity potential and the streamfunction, respectively. Here $(\)_t$ denotes the 'total' solution of the jet flow. The flow of the vortex ring can be obtained either by applying the Cauchy-Riemann condition to the stream function [24], or by direct evaluation using Biot–Savart law [25]. Traditionally [17,24,26], the velocities induced from this flow are computed from the stream function, Ψ :

$$\Psi(z, r) = \frac{\Gamma_v}{2\pi} \sqrt{r_i r} \left[\left(\frac{2}{\sqrt{m}} - \sqrt{m} \right) K(m) - \frac{2}{\sqrt{m}} E(m) \right] \quad (8)$$

where $m = m(r, z)$. Here, Γ_v is the strength of the vortex and $K(m)$ and $E(m)$ are the complete elliptic integrals of the first and second kind, respectively. The velocities can be determined in a standard fashion by differentiating Ψ ,

$$u_v = \frac{1}{r} \frac{\partial \Psi}{\partial r} \quad u_v = -\frac{1}{r} \frac{\partial \Psi}{\partial z} \quad (9)$$

Alternatively, the Biot–Savart law [25,27,28] can be evaluated directly for the filament vortex-ring solution,

$$\vec{u}_v = \frac{\Gamma}{4\pi} \int_0^{2\pi} \frac{d\vec{l} \times (\vec{r} - \vec{r}_i)}{|\vec{r} - \vec{r}_i|^3} d\theta_i \quad (10)$$

where $d\vec{l}$ is the path enclosed by the vortex ring. The entire explicit solution of the filament vortex-ring has recently been developed [29].

2.2. Free surface boundary conditions

The unsteady Bernoulli equation provides the boundary condition along a free surface [30]. This condition provides a connection between the inertial, hydrostatic, and capillary forces at the interface. Because the surface curvature, κ , depends non-linearly on the surface shape, the overall expression is non-linear. Using the non-dimensionalization described previously, the appropriate dimensionless form of the Bernoulli equation is given by:

$$\frac{\partial \phi_t}{\partial t} + \frac{1}{2} |\nabla \phi_t|^2 + P_g + \frac{\kappa}{We} - \frac{Bo}{We} z = 0 \quad (11)$$

where P_g is the dimensionless gas-phase pressure (assumed to be zero in the present studies), and We and Bo are the Weber and Bond numbers,

$$We = \frac{\rho U^2 a}{\sigma} \quad Bo = \frac{\rho g a^2}{\sigma} \quad (12)$$

where σ is the surface tension and g is the gravitational constant. As shown in Fig. 2, the vortex ring is located at the nozzle exit in order to model the vorticity present in the actual flow. While the singularity arises at the vortex ring, the solution at the vortex-ring is also singular and that of

the computational nodes near the vortex-ring is not physical. In an effort to overcome the problem, we have separated the governing equation for potential flow from the total solution; the time derivative of the vortex-ring is zero (i.e. $\partial \phi_v / \partial t = 0$) since its strength (or circulation) is assumed constant and its location is fixed. Thus the time derivative of the Eq. (7) is given by:

$$\frac{\partial \phi_t}{\partial t} = \frac{\partial \phi}{\partial t} \quad (13)$$

Thus Eq. (11) becomes:

$$\frac{\partial \phi}{\partial t} + \frac{1}{2} |\nabla \phi_t|^2 + P_g + \frac{\kappa}{Ee} - \frac{Bo}{We} z = 0 \quad (14)$$

The transformation from the Eulerian (i.e. $\partial/\partial t$) to the Lagrangian (i.e. D/Dt) is required as the computational nodes move respect to time, t :

$$\frac{D\phi}{Dt} = \frac{\partial \phi}{\partial t} + \nabla \phi_t \nabla \phi \quad (15)$$

Combining Eqs. (14) and (15) yields:

$$\frac{D\phi}{Dt} = \nabla \phi_t \nabla \phi - \frac{1}{2} |\nabla \phi_t|^2 - P_g - \frac{\kappa}{We} + \frac{Bo}{We} z \quad (16)$$

Substitution of Eq. (7) into Eq. (16) (for $\nabla \phi$ term) yields:

$$\begin{aligned} \frac{D\phi}{Dt} &= \nabla \phi_t \nabla (\phi_t - \phi_v) - \frac{1}{2} |\nabla \phi_t|^2 - P_g - \frac{\kappa}{We} + \frac{Bo}{We} z \\ &= \nabla \phi_t \nabla \phi_t - \nabla \phi_t \nabla \phi_v - \frac{1}{2} |\nabla \phi_t|^2 - P_g - \frac{\kappa}{We} \\ &\quad + \frac{Bo}{We} z = \frac{1}{2} |\nabla \phi_t|^2 - \nabla \phi_t \nabla \phi_v - P_g - \frac{\kappa}{We} + \frac{Bo}{We} z \end{aligned} \quad (17)$$

Since differential operator (∇) is a linear function, superposition theory holds for the velocity as well:

$$u_t = u + u_v \quad v_t = v + v_v \quad (18)$$

Combining Eqs. (17) and (18), we obtain more explicit Bernoulli relation for ϕ :

$$\frac{D\phi}{Dt} = \frac{1}{2} |u_t|^2 - \vec{u}_t \vec{u}_v - \frac{\kappa}{We} - P_g + \frac{Bo}{We} z \quad (19)$$

Now that we have separated the ϕ from the general solution ϕ_t , the entire time marching of the numerical algorithm is related to ϕ only. The effect of the vortex ring comes into play only in Eq. (18). Bernoulli's Eq. (19) is the 'non-linear' boundary condition for the Laplace equation and it is marched in time using a fourth order Runge-Kutta time integration.

The curvature of the highly distorted surface is determined with fourth-order accuracy [31,32]. We have used the curvature definition from Smirnov [33]:

$$\kappa = \frac{1}{r} \left(\frac{\partial z}{\partial s} \right) + \left(\frac{\partial r}{\partial s} \right) \left(\frac{\partial^2 z}{\partial s^2} \right) - \left(\frac{\partial^2 r}{\partial s^2} \right) \left(\frac{\partial z}{\partial s} \right) \quad (20)$$

The derivatives are evaluated using central differencing with the exception of the ends of the domain where forward or backward derivatives are applied [32].

The location of nodes on the free surface (i.e. z and r) is advanced by integrating the respective velocity components in time:

$$\frac{Dz}{Dt} = \frac{\partial \phi}{\partial z} \quad \frac{Dr}{Dt} = \frac{\partial \phi}{\partial r} \quad (21)$$

where

$$\frac{\partial \phi}{\partial z} = \frac{\partial \phi}{\partial s} \cos \beta - q \sin \beta \quad (22)$$

$$\frac{\partial \phi}{\partial r} = \frac{\partial \phi}{\partial s} \sin \beta + q \cos \beta$$

where $q = \partial \phi / \partial n$ is the normal derivative of ϕ . The surface slope, β , is assumed to be given by the slope of the parabola at the middle node [31].

2.3. Smoothing

Nodes are repositioned along the distorted surface using cubic splines [34], and nodes can be added (due to fluid exiting the nozzle) or removed (due to atomization events) without user intervention. The current ‘high-speed’ atomization simulation is more susceptible to numerical instability than the low-speed atomization (i.e. varicose breakup simulation with smooth surface) due to complex surface shape. In addition, the ‘necking’ region where a droplet is pinched-off experiences a relatively high velocity (i.e. node velocities reach 2–7 times that of the jet speed) and therefore ‘node-crossing’ or ‘not-simply-connected domain’ sometimes occurs. Thus numerical smoothing is crucial to prevent the numerical instability [35].

Following the definition for filter function and its transfer function by Spyropoulos and Blaisdell [36]:

$$\hat{f}_j = \sum_{n=0}^{N-1} a_n \frac{f_{j-n} + f_{j+n}}{2} \quad G_k = \sum_{n=0}^{N-1} a_n \cos\left(\frac{2\pi kn}{N}\right) \quad (23)$$

where \hat{f} is the filtered function, f is the function prior to the filtering, a_n is the coefficient listed in Table 1 for $N = 2-4$,

Table 1
Coefficients for the various explicit filter functions

	N	a_0	A_1	a_2	a_3
3-pt Trapezoid	2	0.5	0.5	–	–
5-pt Hilbing et al. [37]	3	0.9625	0.05	–0.0125	–
5-pt Lundgren and Mansour [11]	3	0.94	0.08	–0.02	–
5-pt Longuet-Higgin and Cokelet [35]	3	0.625	0.5	–0.125	–
7-pt Lele [38]	4	0.5	0.5625	–	–0.0625
7-pt Spyropoulos and Blaisdell [36]	4	0.5	0.6744132	–	–0.1744132

N is the number of points used, G_k is the filter transfer function, and k is the wavenumber. Table 1 provides the coefficients for the various explicit filter functions developed by researchers [11,35–38]. In Fig. 6, the transfer filter function, G_k , is plotted as a function of the wavenumber, $2k/N$. The main purpose of using filter is to suppress the relatively large wavenumbers (or small wavelengths). The filters by Hilbing et al. [37] and Lundgren and Mansour are not suitable because they do not suppress large wavenumbers sufficiently. The filter by Spyropoulos and Blaisdell [36] is not suitable either as it amplifies some wavenumbers. Since the 3-pt trapezoid filter damps out the small wavenumbers more than other comparable filters, it may be too diffusive for the current use. While we hope to damp out the large wavenumbers and leave the small wavenumbers as they are, we have chosen the filter function by Longuet-Higgins and Cokelet [35]; this filter is designed to eliminate the odd-even mode in the function which contains the highest frequency, known as the Nyquist Rate [39].

2.4. Vorticity centroid

The centroid of vorticity of the viscous flow is regarded as the center of the vortex-ring. The definition of the centroid of the vorticity, weighted in the radial direction is given by:

$$\vec{r} = \frac{\int_{r=0}^{r=1} r \omega \, dr}{\int_{r=0}^{r=1} \omega \, dr} \quad (24)$$

and the vorticity, ω , is defined as:

$$\omega = \frac{\partial v}{\partial z} = \frac{\partial u}{\partial r} \quad (25)$$

where u and v are the velocities in the axial and radial direction, respectively. Assuming $\partial v / \partial z \approx 0$, i.e. parallel flow at the orifice exit plane, the centroid can be written as:

$$\vec{r} = \frac{\int_{u(r=0)}^{u(r=1)} r \, du}{\int_{u(r=0)}^{u(r=1)} du} \quad (26)$$

Substituting the definition of the displacement thickness, δ_1 , [40] into Eq. (26) and applying integration by parts gives the following result:

$$\vec{r} = 1 - \delta_1 \quad (27)$$

where

$$\delta_1 = \int_0^1 \left(1 - \frac{u(r)}{U}\right) dr \quad (28)$$

δ_1 can be approximated using a Navier–Stokes solution of the internal flow, or appropriate analytical methods such as

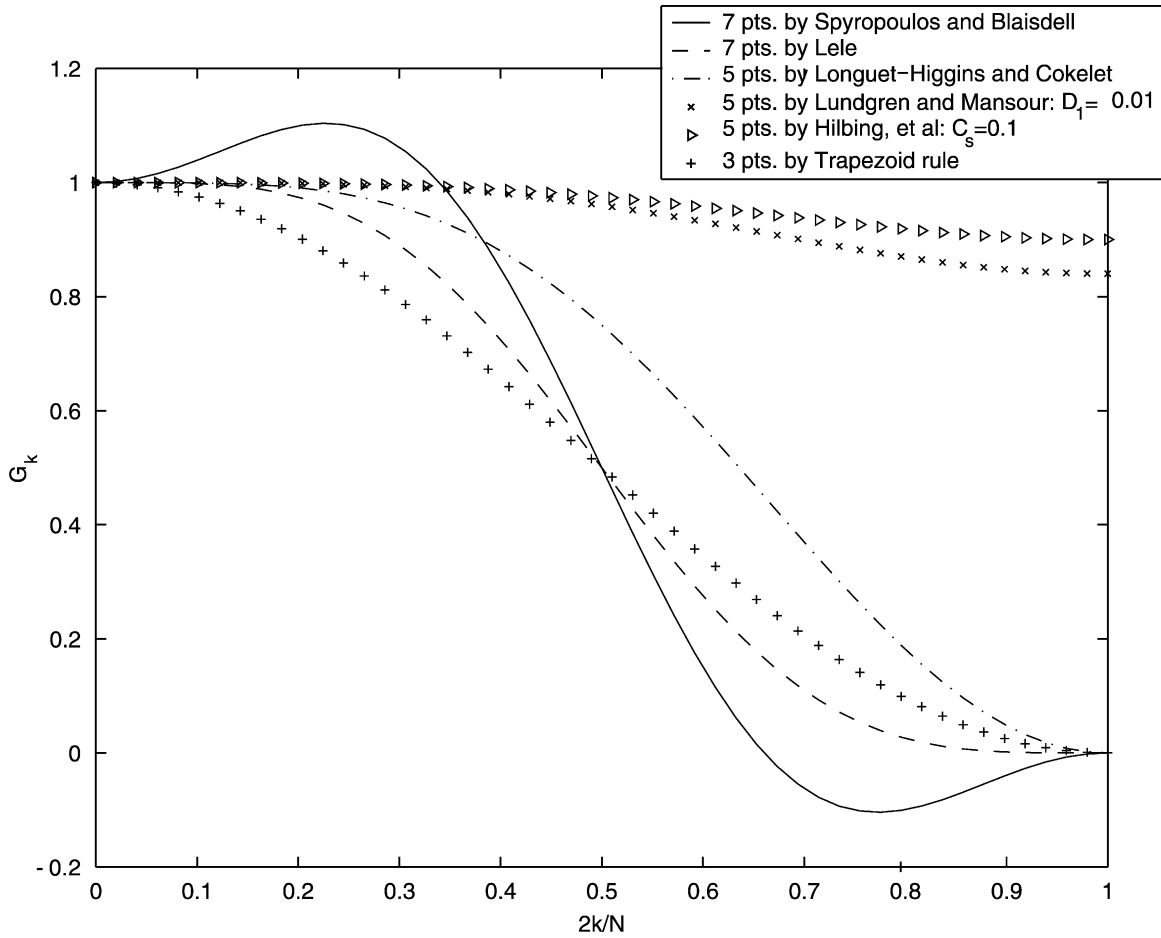


Fig. 6. Filter transfer function vs. wavenumber for various filters.

Blasius solution [40] for a flat-plate or the Thwaites' [41] equation for a converging/diverging nozzle.

The vortex strength Γ_v is defined as the circulation around any path enclosing the vortex-ring, namely:

$$\Gamma_v = \oint \vec{u} d\vec{l} \tag{29}$$

where \vec{u} is the internal flow velocity of the injector orifice and \vec{l} is the integration path. The integration is taken in a counterclockwise direction around the path. Assuming $\partial u/\partial z = 0$ and a no-slip boundary condition at the wall, the surface integral in Eq. (29) can be written as follows for the path we have chosen:

$$\Gamma_v = \Delta z \tag{30}$$

where Δz is the length scale which is comparable to the most dominant wavelength, λ . Γ_v is always positive and will induce counterclockwise motion (this is based on the upper half of the flow going from left to right). Eqs. (27) and (30) uniquely determine the location and strength of the vortex from first principles. No additional calibration constants are used in the formulation.

It is possible to set $\Delta z = \lambda$, predicted by Brennen's result [42], since the circulation causes the axisymmetrically

disturbed wavelength observed at the nozzle exit. The λ observed in Hoyt and Taylor's case [16] is a function of the momentum thickness δ_2 , scaled by the parameter $\gamma = 0.175$. Presuming a high contraction ratio of the nozzle reduces the turbulence fluctuation, Hoyt and Taylor [16] assumed a laminarized flow over a flat plate and therefore they utilized the Blasius [40] solution to approximate the momentum thickness, namely:

$$\Gamma_v = \lambda = \left(\frac{2\pi}{0.175} \right) \delta_2 \tag{31}$$

Another possible choice for the circulation approximation is to use the Kutta-condition [30] from the potential flow theory. It is known that the velocity of the potential flow at a sharp corner is infinite and therefore it is not physically possible. One remedial treatment is that a stagnation point is forced at the sharp corner, known as the 'Kutta-condition'. While the gradient of the inflow velocity of the injector orifice is zero due to the nature of potential flow, one may adjust the strength of vortex-ring Γ_v to be such that the sum of potential velocity and vortex induced velocity in the axial direction to be zero at the sharp corner; this linear relation was applied and solved to find the Γ_v . The closer the vortex-ring is to the wall (i.e. the higher \vec{r}), the stronger the vortex

induced velocity will be. In order to satisfy the stagnant velocity at the sharp corner with constant potential inflow velocity of 1.0, Γ_v must decrease as \bar{r} increases. It is shown in Fig. 7 that the strength of the vortex-ring condition decreases as \bar{r} increases. One may utilize the cubically interpolated equation of the Kutta-condition in Fig. 7.

The third possible choice is to adjust the strength to be such that the vorticity integral over the radial direction of the real flow matches that of the vortex-ring:

$$\int_{r=0}^{r=1} \omega \, dr = \int_{r=0}^{r=1} \omega_v \, dr \tag{32}$$

It is known that ω_v is infinite at the ring and zero everywhere else. However, the change in the induced axial-velocity over the radial direction is finite (i.e. $\partial u_v / \partial r$). Thus we again assume a parallel flow for the real flow (i.e. $\partial v / \partial z = 0$). Then Eq. (32) becomes:

$$\int_{u(r=0)}^{u(r=1)} du = \int_{u_v(r=0)}^{u_v(r=1)} du_v \tag{33}$$

This is essentially matching Δu_v to be U and will yield the positive Γ_v . The quadratic interpolation of this approximation is shown in Fig. 7.

The variation of Γ_v as a function of the centroid of the vorticity \bar{r} is shown in Fig. 7. It is seen that the Γ_v used is lower than that of the Kutta-condition. The ratio of their Γ_v value varies from 2.8 to 1.0 as a function of \bar{r} . It is observed that their difference in Γ_v decreases as \bar{r} increases and eventually yields difference of approximately 3% from one to the other at about $\bar{r} = 0.99$. The reason for such a behavior is that the model accuracy improves when the boundary layer is ‘thin’.

In summary, any choice of the three methods is applicable for the circulation approximation not only because Γ_v differs little at high \bar{r} but also because Γ_v by itself does not change the droplet size significantly. However, one needs to use the same approximation consistently when parametric studies are performed. We have used the approximation using Brennen’s theory for the case presented Section 3.

2.5. Post-processing formulation for droplets

The addition of the Biot–Savart Law to the inviscid jet of the BEM formulation is expected to cause instability at the free surface that eventually forms a series of toroidal

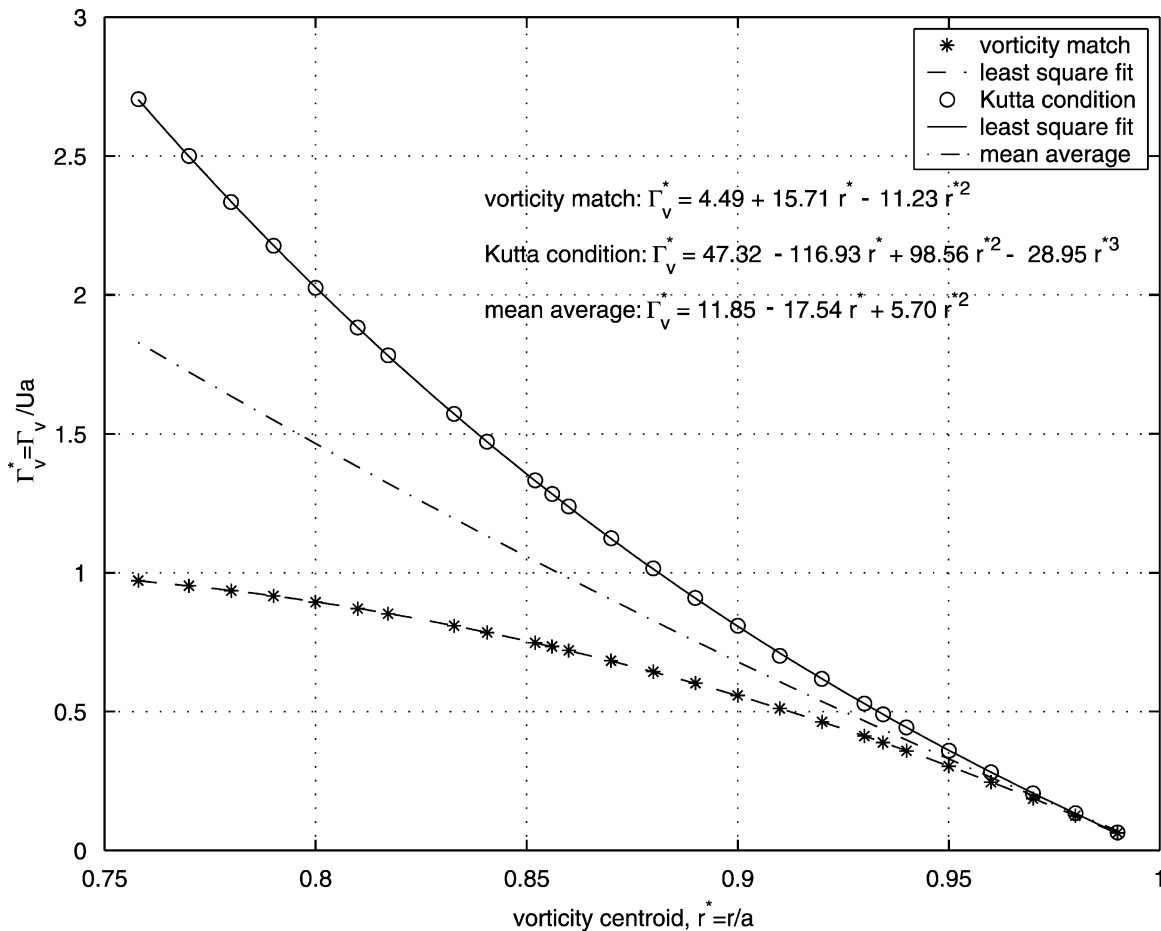


Fig. 7. General approximation of circulation for filament vortex-ring using the Kutta condition and vorticity-match method.

ligaments pinched off from the main body of the jet. Here the formulations for the cross-sectional area, centroids of the area, volume, and the velocity of the droplets are developed.

Using Gauss’s divergence theorem, we have transformed the surface integral to a line or contour integral in order to compute the cross-sectional area of a pinched-off ring:

$$A = \frac{1}{2} \left[\int_C r \, dz + \int_C z \, dr \right] \tag{34}$$

which was discretized using the trapezoid Rule,

$$A = \frac{1}{4} \sum_{j=1}^N [(r_j + r_{j+1})(z_{j+1} - z_j) - (z_j + z_{j+1})(r_{j+1} - r_j)] \tag{35}$$

where N is the last (or maximum) node that closes the loop. The centroids of the cross-sectional area are defined as:

$$z_c = \frac{\int_S z \, dA}{A} \quad r_c = \frac{\int_S r \, dA}{A} \tag{36}$$

This is also discretized using the trapezoid Rule. Similar to the previous approach, we have found the cross-sectional area can be expressed as:

$$z_c = \frac{1}{12A} \sum_{j=1}^N [(r_j + r_{j+1})(z_{j+1}^2 - z_j^2) - (z_j + z_{j+1})^2(r_{j+1} - r_j)] \tag{37}$$

$$r_c = \frac{1}{12A} \sum_{j=1}^N [(r_j + r_{j+1})^2(z_{j+1} - z_j) - (z_j + z_{j+1})(r_{j+1}^2 - r_j^2)] \tag{38}$$

The theorem of Pappus–Guldinus [43] relates a volume of revolution to its generating cross-sectional area:

$$V = 2\pi A r_c \tag{39}$$

For the velocities of a droplet, we have weighted both velocities u_D (axial) and v_D (radial) in the radial direction. The formulation is as follows:

$$u_D = \frac{\sum_{j=1}^N \left(\frac{\partial \phi}{\partial z} \right)_j r_j}{r_c N} \quad v_D = \frac{\sum_{j=1}^N \left(\frac{\partial \phi}{\partial r} \right)_j r_j}{r_c N} \tag{40}$$

2.6. Modeling secondary instability

While the current model is based on an axisymmetric formulation, actual primary atomization is a three-dimensional phenomenon (see Fig. 8(a)). The model result of pinch-off, as shown in Fig. 8(b), is not a droplet but a vortex-ring with a significant amount of circulation around the ring surface. The circulation around the ring surface is large enough to cause instability in the circumferential direction. In reality, this is the secondary instability which occurs

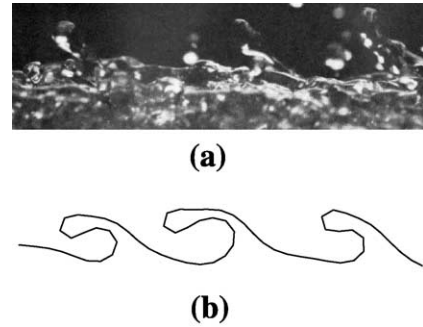


Fig. 8. (a) Closeup of the actual Hoyt and Taylor’s water jet [46]. Printed under the permission of Journal of Fluid Mechanics. (b) The closeup of the model result for Hoyt and Taylor’s water jet.

before the vortex-ring pinch-off. The current model assumes that droplets are formed from a secondary instability on annular ligaments shed from the periphery of the jet. This amounts to a decoupling of primary and secondary instability which permits the axisymmetric analysis of the jet itself.

Ponstein [1] investigated the linear stability of a liquid column with circulation Γ_r and radius a_r . Ponstein’s result is utilized to predict the dominant wavelength k in the circumferential direction:

$$\omega^2 = \left[\frac{1 - k^2}{We_r} + \left(\frac{\Gamma_r}{2\pi} \right)^2 \right] k \frac{I_1(k)}{I_0(k)} \tag{41}$$

where $We_r = \rho U^2 a_r / \sigma$. Note that the ring radius, a_r , is the non-dimensional variable. This expression is solved to determine the $k = k_{max}$ value attributed to the maximum growth rate, ω for a given ring geometry and circulation. Since Ponstein’s analysis was conducted for a liquid column, we assume that the thickness of the ring-shaped ligaments is much less than the nozzle/jet radius (i.e. $a_r \ll a$). This assumption is confirmed from ligament sizes produced in the calculations. Fig. 9 shows how Ponstein’s equation is applied to the vortex-ring (annular ligament) with circulation Γ_r .

At the event of vortex-ring pinch-off, all information about the ring is collected (i.e. volume, centroids, etc). Thus we can calculate the circumferential length of the ring, $l = 2\pi r_c$. The most dominant wavelength ($\lambda = 2\pi/k_{max}$) which

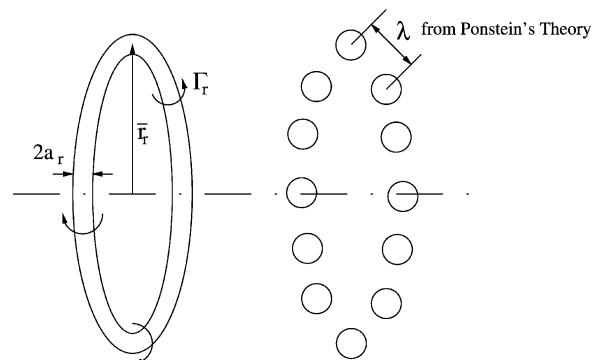


Fig. 9. Application of Ponstein’s [1] theory for the secondary instability of a pinch-off vortex-ring.

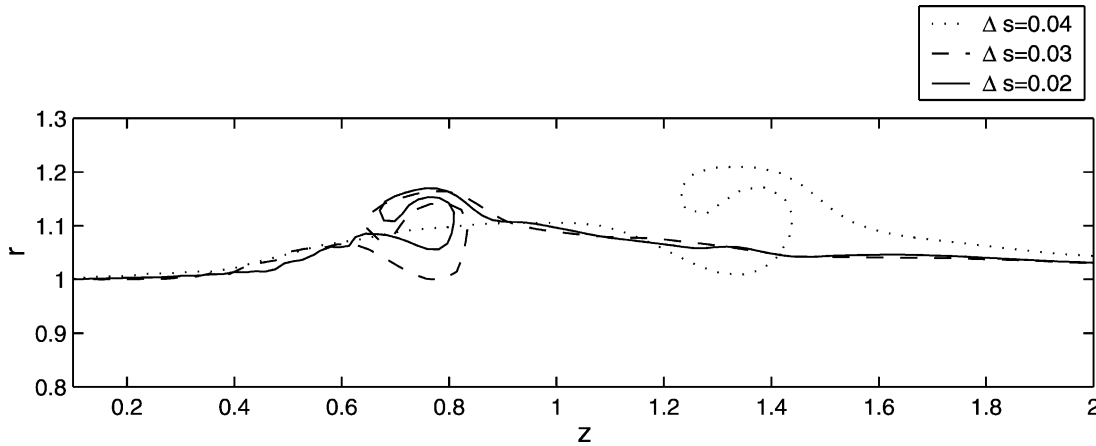


Fig. 10. Grid convergence study: effect of nodal spacing, Δs .

corresponds to the maximum growth rate is known from Ponstein's Eq. (41). Thus the number of droplets per ring can be estimated (i.e. $N_D = l/\lambda$). The volume of the ring (i.e. V) is known and that of a droplet can be approximated using the definition of a sphere volume, $V_D = V/N_D = \frac{4}{3}\pi(D/2)^3$. Thus a droplet diameter (D) can be estimated.

3. Results

3.1. Grid convergence study

Hoyt and Taylor's case is used for the grid convergence check (i.e. $We = 19,057$, $\bar{r} = 0.99$, and $\Gamma_v = 0.139$). Δs is the grid spacing for the BEM node. While Hilbing [32] mentioned that $\Delta s = 0.300$ is fine enough to resolve the low speed 'Rayleigh breakup' where waves are of length comparable to the orifice diameter, a much finer grid resolution is required for high speed atomization where the wavelengths are comparable to the boundary layer thickness at the orifice exit. For this reason, the grid resolution for the present studies taxes the current computational capabilities of even advanced Linux-based compute clusters. In Fig. 10, it is shown that the axial location for the first ring pinch-off is reasonably insensitive to mesh spacing for $\Delta s \lesssim 0.030$. However, grid function convergence studies indicate that a smaller mesh spacing is required for the accurate prediction of the droplet characteristics in the atomization regime. About 1000–3000 droplets were collected for each run for

Table 2
Grid convergence test

Δs	\bar{N}_D/ring	Standard deviation	SMD/d	\bar{u}_D	\bar{v}_D	\bar{U}_D
0.050	10.07	4.68	0.0995	0.608	0.442	0.752
0.040	10.87	8.71	0.0962	0.689	0.430	0.812
0.030	14.20	11.33	0.0841	0.790	0.479	0.924
0.020	12.46	8.46	0.0729	0.770	0.419	0.876
0.016	10.44	6.65	0.0623	0.779	0.404	0.877
0.012	10.87	6.44	0.0588	0.796	0.411	0.896

statistically reliable data and results for drop statistics are shown in Table 2. The Sauter Mean Diameter, SMD, (drop whose diameter replicates the average surface area of drops in the population) is the most frequent measure used in the atomization field. Table 2 shows that the \bar{N}_D per ring, its Standard Deviation, and SMD are converged to a reasonable accuracy at $\Delta s = 0.012$. Thus we have used $\Delta s = 0.01016$. In addition, the standard deviation of \bar{N}_D/ring does not change much after $\Delta s \lesssim 0.016$. Similarly, the time-averaged droplet velocities (i.e. \bar{u}_D and \bar{v}_D) do not change much either for this mesh spacing. This result also validates the pinch criteria employed for a ligament breakup: a pinch-off is assumed when the distance between binary nodes is less than a certain tolerance, ϵ . The range of the tolerance is 20–70% of the mesh spacing. The ligament size is also insensitive to the range of the pinch-off criteria.

It is uncertain when to stop the simulation since the jet can grow indefinitely depending on injection conditions. For the simulations conducted to date, the time required for the first pinching event is typically around $t \approx 1.7$. We found that collecting about 300–400 rings provides stastically reliable data. This would give roughly 1000 droplets. Thus we typically stop our calculation at about $t \approx 5.0$. Table 3 shows that the solution is insensitive to what for $t > 4.0$.

3.2. Effect of Rankine vortex size and initial jet length

In Fig. 1, vortices induce motion/instability near to the nozzle exit (i.e. axisymmetrically disturbed waves) and eventually cause the jet to break up into turbulent flow. However, the flow at the nozzle exit is nearly laminar

Table 3
Effect of calculation length on drop statistics

t	SMD/d	N_D	\bar{N}_D/ring	Standard deviation
2.0	0.0628	88	7.97	3.329
3.0	0.0623	856	10.44	6.665
4.0	0.0635	2582	11.08	7.936
5.0	0.0655	5132	11.48	7.985

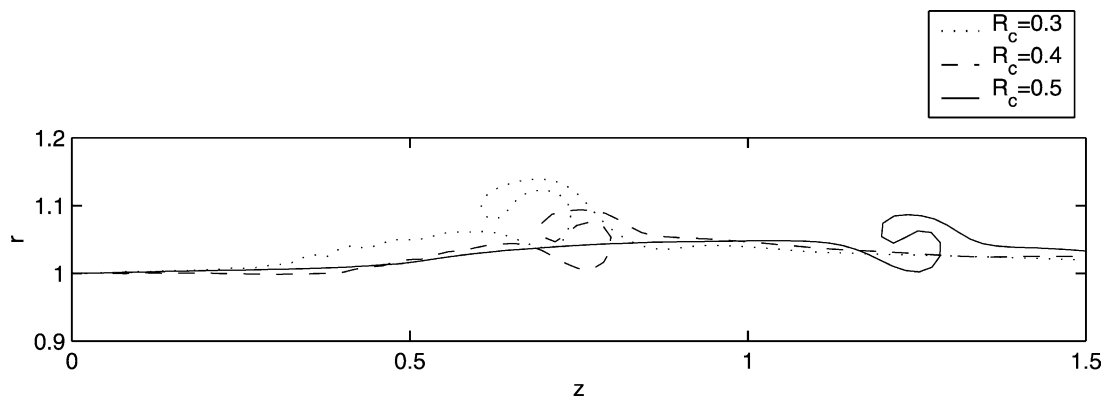


Fig. 11. Effect of the size of the Rankine vortex, R_c .

flow as the flow is laminarized through highly contracted nozzle geometry under a favorable pressure gradient [16]. Since the filament vortex-ring is located exactly at the nozzle exit, the computational nodes near the nozzle exit are induced with the greater motion. This seems contradictory to the observed laminarized flow as shown in Fig. 1. In reality, it takes some time and distance for the rollup motion to develop and therefore the relaxation length is present regardless of the flow regime. For this reason, a cutoff for the superimposition method of the filament vortex-ring is introduced using stationary Rankine vortex model [17]. The size of Rankine vortex (i.e. R_c in Fig. 2), whose center is located at the upper corner of the nozzle exit, has little effect on droplet size and thus this is the parameter that can be set at the users convenience. As shown in Fig. 11, little variation in the axial pinch-off location is observed for $R_c < 0.4$. We have set $R_c = 0.3$ so that the computational nodes at the near nozzle exit are not affected by the induced motion. This is essentially setting the Rankine vortex size to be the relaxation length, $R_c \approx l_r$. It should be noted that

the relaxation length can be scaled with the nozzle length, l [44,45].

The simulation begins with an initially assumed jet shape as shown in Fig. 2. The size of the initial shape seems to have some effect on the first pinch-off. The larger the shape, the earlier the motion/instability is induced. However, the initial shape size seems to have little effect on the axial pinch-off location as shown in Fig. 12.

3.3. Comparison with experiment

The complete simulation of the Hoyt and Taylor's jet [46] is shown in Fig. 13. The jet structure is initially assumed to be a simple cylinder with a hemispherical tip as shown in Fig. 2 and its evolution is simulated via time integration. The simulation is completed at $t = 5.0$. A slight 'swelling' is observed at $t = 1.0$ and the fluctuation of the jet surface is seen at $t > 2.0$. The velocities induced by the bound vortex are large enough to penetrate the jet surface and it results in the primary atomization. It should be noted that most liquid ligaments, pinching from the jet surface, are in the 'rollup'

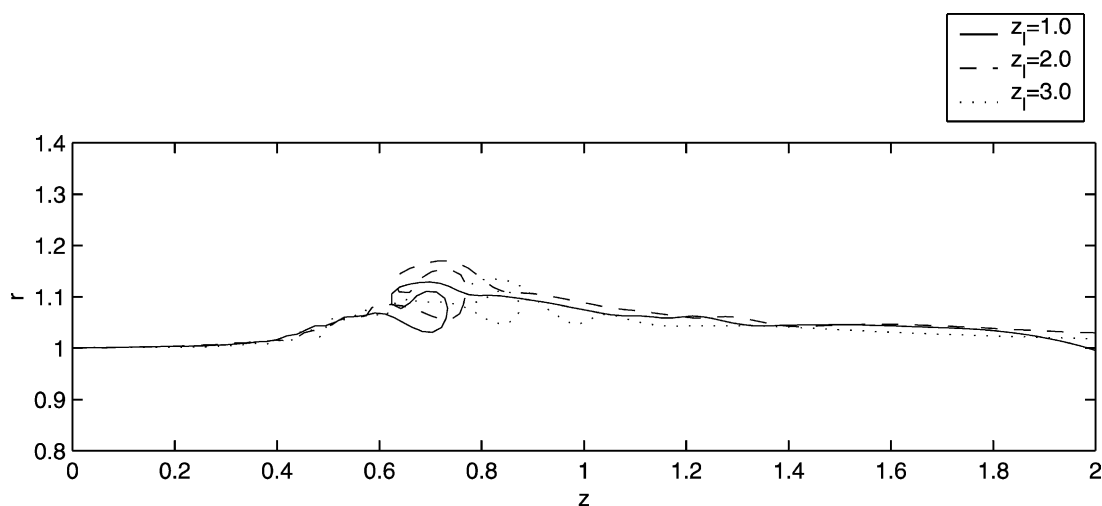


Fig. 12. Effect of the initially assumed shape.

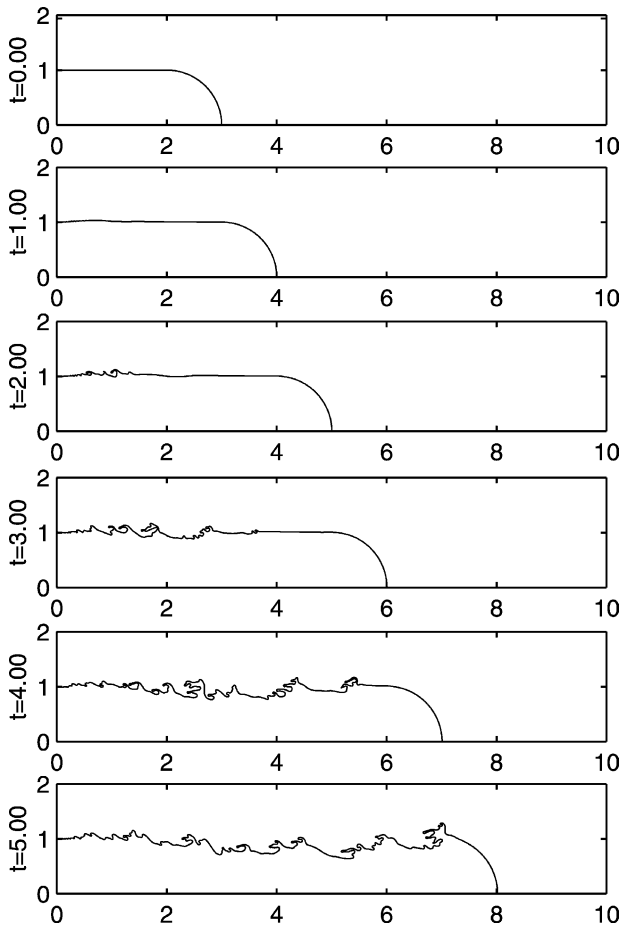


Fig. 13. Jet evolution for conditions consistent with Hoyt and Taylor's experiment [46]. Annular ligaments which have pinched off from the domain are not shown to improve clarity.

motion in counterclockwise direction while the mean velocity of the ligament is in the streamwise direction. Similar structures are noted in Fig. 8(a) in a closeup view of the Hoyt and Taylor experiment. The counterclockwise rollup motion is a strong evidence that the boundary layer instability is the fundamental cause of the primary atomization. The mean velocity of most droplets are in streamwise direction as the droplets motion propagates along with the main jet stream, the most dominant convective source.

It was mentioned, in Section 3.2, that the model takes advantage of Ponstein's Eq. (41) to model the instability of a pinch-off vortex-ring. Using the Eq. (41), the number of waves or droplets (N_D) per ring is predicted and plotted as a function of the circulation, Γ_r . Their relationship is parabolic and the least square fit is available in Fig. 14. Thus if Γ_r is known, a rough estimation of ND can be produced. Fig. 15 shows the relation between the number of circumferential waves and the core size of a pinch-off vortex-ring. As the size increases, more waves appear. This is exactly the opposite phenomenon as for the elliptical instability of Widnall [47] and Sullivan: they observed more waves when the core size decreases. It should be noted that the mechanism of the surface tension driven instability

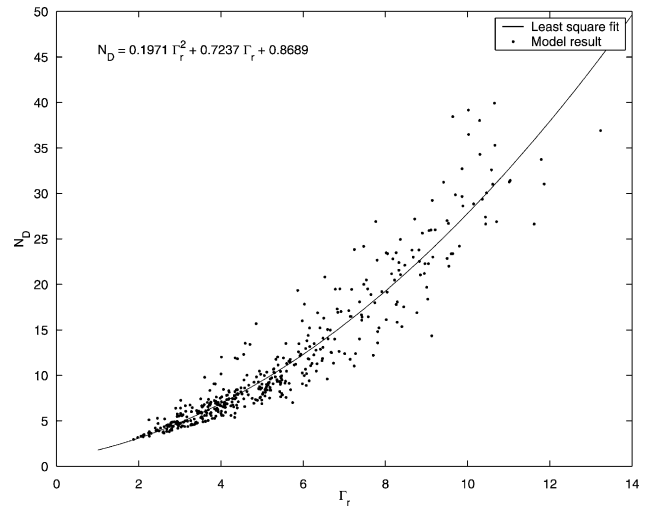


Fig. 14. Prediction of circumferential wave number (or number of droplet) due to circulation around the rotating ring pinched-off from the main liquid stream.

(i. e. liquid vortex-ring in air) is different from the shear layer driven elliptical instability [48–51], (i.e. liquid into liquid or gas into gas).

It is well known that the droplet size varies significantly within the atomization regime. Wu et al. [52] reported the droplet size variation with U for the turbulent water jet into air. Hoyt and Taylor's experiment had been carried out for the Bernoulli pressure $\Delta P < 60$ psi; no result with higher ΔP is reported [16,46,53]. However, we hypothesized the increase in ΔP for the Hoyt and Taylor jet. The result is taken the jet speed up to $U = 40$ m/s which corresponds to $\Delta P \approx 116$ psi or slightly higher in order to account for some pressure loss within the nozzle. The final result for the Hoyt and Taylor's case [46] is shown in Fig. 16. Using the methodology employed in the previous section with no calibration constants, the model predicts the Sauter Mean Diameter, SMD, with reasonable accuracy. As shown in Fig. 16, there is a steep gradient at a jet speed around $U \approx 20$ m/s for the Wu et al. [52] turbulent jet experiment. Our model

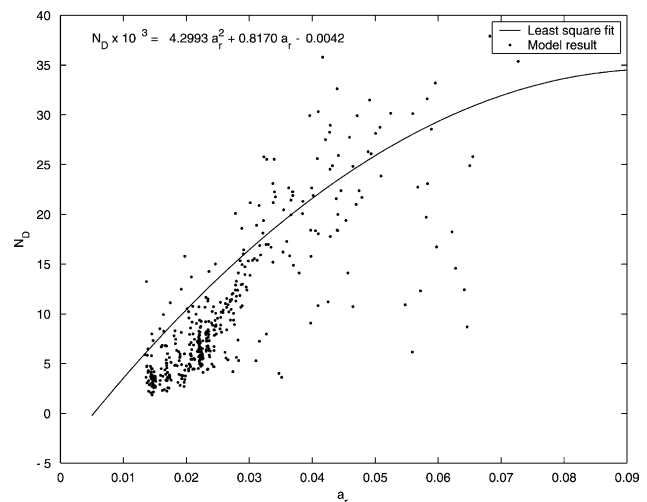


Fig. 15. Number of waves vs. core thickness of pinch-off vortex-ring.

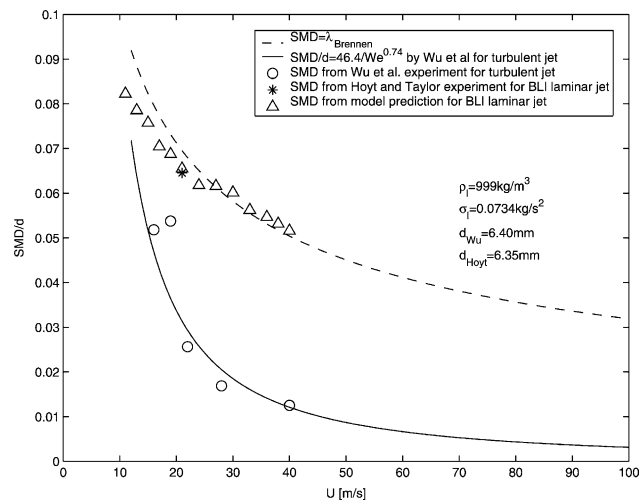


Fig. 16. Sauter mean diameter comparison for various jet speed U in [m/s].

result overlaps with that obtained by Hoyt and Taylor. It is interesting to observe that Wu et al.'s data is also similar to our result and that of Hoyt and Taylor at about $U \approx 20$ m/s. While Wu et al. noted this as the region of 'uncertainty', it is possible that the rollup motion was competing with the turbulence and thus the perceptible effect of the rollup motion appears as shown in Fig. 16.

For $U \gtrsim 20$ m/s, differences between the calculations and the experiments emerge. It is known that linear analysis [54] overpredicts the droplet size (by less than 20%) because it neglects the satellite droplet mass due to the non-linear effect [55,56] which yields the multiple crests per wavelength. Ponstein's Eq. (41) is a linear analysis and thus it also tends to overpredict the droplet size. However, a 20% or smaller SMD difference does not explain the difference we see in Fig. 16 at a higher jet speed. This is due to the fundamental difference between the boundary layer instability jet and the turbulent jet: the boundary layer instability jet is scaled by the momentum thickness [42] and the turbulent jet is scaled by the Kolmogorov length scale, l_k or/and turbulence eddy characteristics length of kinetic energy, l_i [52]. Wu et al. derived the empirical formula using the 'surface kinetic energy' argument which gives SMD scaled by $\sim 1/U^{1.48}$. Thus the governing length scale (i.e. l_k and l_i) decrease significantly at about $U \sim 20$ m/s. On the other hand, the SMD of the boundary layer instability jet is scaled by δ_2 : $SMD \sim 1/U^{0.5}$ and thus its change with respect to U is relatively moderate as shown in Fig. 16.

Another experiment on the boundary layer instability jet is available by McCarthy and Molloy [57]. The rollup motion causes the jet to be atomized when the circulation is large enough to win against other competing forces such as viscous or/and capillary forces. In Fig. 17(a), the 'stretching' is observed due to capillary force when the jet is atomized. In Fig. 17(b), the computational result for the case is shown where the similar stretching of the capillary force is observed. For the high-speed jet, like that of Hoyt and

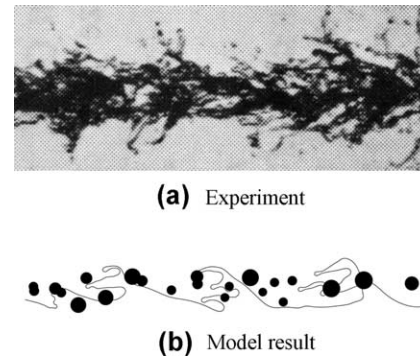


Fig. 17. Liquid: 60% glycerol and 40% water by weight, $\rho = 103$ kg/m³, $\mu = 11$ cP, $\sigma = 0.0669$ kg/s², $U = 20$ m/s, $d = 2.54$ mm, $We = 781$, $Re = 4750$. Comparison between experiment [57] and model results. The black circles represent the location and the relative size of the pinched-off droplets. Printed under the permission of Elsevier Science.

Taylor [16,46], the effect of viscosity and capillary force is of little importance because the jet is nearly inviscid. In fact, the large scale motion of Hoyt and Taylor's jet is governed by the Rayleigh inviscid analysis [54] which concludes the most dominant wavelength to be $\lambda = 4.51d$.

4. Conclusions

A fully non-linear model has been developed to simulate primary atomization caused by boundary layer instability using superposition of a ring vortex with a potential jet flow. The axisymmetric model employs a boundary element methodology in which the vorticity in the boundary layer at the orifice exit is used to determine ring vortex strength and radial location at the orifice exit plane. Annular ligaments are pinched off the surface in this case; a secondary linear instability analysis due to Ponstein is used to predict the fractionization of the ligaments into individual droplets.

The SMD of the model result agrees well with the actual droplet size of Hoyt and Taylor's experiment. The result of the current model is also compared with the experimental data of Wu et al. [52]. The comparison confirms that the current model predicts the droplet size satisfactorily.

Acknowledgements

The authors gratefully acknowledge the support of Dr Mitat Birkan and the AFOSR under grant number F49620-99-1-0092.

References

- [1] Ponstein J. Instability of rotating cylindrical jets. Appl. Scientific Res. 1959;8(6):425–56.
- [2] Hilbing JH, Heister SD. Droplet size control in liquid jet breakup. Phys. Fluids 1996;8(6):1574–81.

- [3] Hilbing JH, Heister SD. Nonlinear simulation of a high-speed, viscous liquid jet. *Atomization Sprays* 1997;2:1–24.
- [4] Heister SD, Rutz M, Hilbing JH. Effect of acoustic perturbations on liquid jet atomization. *J. Propulsion Power* 1997;13:82–8.
- [5] Rump K, Heister SD. Modeling the effect of unsteady chamber conditions on atomization processes. *J. Propulsion Power* 1998;14: 576–8.
- [6] Heister SD. Boundary element methods for two-fluid free surface flows. *Engng Anal. Boundary Elements* 1997;19:309–17.
- [7] Kamiya N, Nakayama K. Prediction of free surface of die swell using the boundary element method. *Comput. Struct.* 1993;46:387–95.
- [8] Kelmanson MA. Boundary integral equation solution of viscous flows with free surfaces. *J. Engng Math.* 1983;17:329–43.
- [9] Tanzosh J, Manga M, Stone HA. Boundary integral methods for viscous free-boundary problems: deformation of single and multiple fluid–fluid interfaces. In: Brebbia CA, Ingber MS, editors. *Boundary Element Technology*, vol. VII.; 1992. p. 19–39.
- [10] Mansour NN, Lundgren TT. Satellite formation in capillary jet breakup. *Phys. Fluids* 1990;2:1141–4.
- [11] Lundgren TT, Mansour NN. Oscillations of drops in zero gravity with weak viscous effects. *J. Fluid Mech.* 1988;194:479–510.
- [12] Murray IF, Heister SD. On a droplet's response to acoustic excitation. *Int. J. Multiphase Flow* 1999;25:531–50.
- [13] Yoon SS, Heister SD, Epperson JT, Sojka PE. Modeling multi-jet mode electrostatic atomization using boundary element methods. *J. Electrostat.* 2001;50:91–108.
- [14] Setiawan E, Heister SD. Nonlinear modeling of an infinite electrified jet. *J. Electrostat.* 1997;42:243–57.
- [15] Shkadov VY. Wave formation on surface of viscous liquid due to tangential stress. *Fluid Dyn.* 1970;5:473–6.
- [16] Hoyt JW, Taylor JJ. Turbulence structure in a water jet discharging in air. *Phys. Fluids* 1977;20(10):S253–7.
- [17] Saffman PG. *Vortex Dynamics*. New York: Cambridge University Press; 1992. p. 22, 192–5.
- [18] Liggett JA, Liu PL-F. *The Boundary Integral Equation Method for Porous Media Flow*. London: George Allen and Unwin; 1983.
- [19] Abramowitz M, Stegun FA. *Handbook of Mathematical Functions*. New York: Dover Publications; 1972. p. 562–6 and 590–2.
- [20] Yoon SS, Heister SD. A fully nonlinear primary atomization. In 15th Annual Conference on Liquid Atomization and Spray Systems, ILASS, held in Madison, Wisconsin; 2002. p. 36–40.
- [21] Yoon SS, Heister SD. A fully nonlinear primary atomization. In 38th AIAA/ASME/SAE/ASEE Joint Propulsion Conference and Exhibit, AIAA, held in Indianapolis, IN; 2002. p. 2002–4179.
- [22] Blackford LS, Choi J, Cleary A, D'A'Azevedo E, Demmel J, Dhillon I, Dongarra J, Hammarling S, Henry G, Petitet A, Stanley K, Walker D, Whaley RC. Department of Computer Science. University of Tennessee, Knoxville; 1997. <http://www.netlib.org/scalapack/index.html>
- [23] Press WH, Teukolsky SA, Vetterling WT, Flannery BP. *Numerical Recipes in FORTRAN. The Art of Scientific Computing*, New York: Cambridge University Press; 1992.
- [24] Lamb H. *Hydrodynamics*. New York: Dover; 1879. p. 236–9.
- [25] Karamcheti K. *Principles of ideal-fluid aerodynamics*. New York: Wiley; 1966. pp. 526–30, 599.
- [26] Batchelor GK. *An introduction to fluid dynamics*. New York: Cambridge University Press; 1999. pp. 511–7, 521–6.
- [27] Duncan WJ, Thom AS, Young AD. *An elementary treatise on the mechanics of fluids*. London: Edward Arnold; 1960. p. 93–4.
- [28] Ramsey AS. *A treatise on hydromechanics*. London: G. Bell and Sons; 1920. pp. 241–4.
- [29] Yoon SS, Heister SD. Analytic solutions for computing velocities induced from potential vortex ring. *AIAA Journal Technical Paper*; 2002. submitted.
- [30] Currie IG. *Fundamental mechanics of fluids*, 2nd ed. New York: McGraw-Hill; 1993. p. 172–4.
- [31] Medina DE. On droplets and boundary elements. Sibley School of Mechanical and Aerospace Engineering, Cornell University, Technical Report FDA-89-12, Ithaca, New York; 1989.
- [32] Hilbing JH. Nonlinear modeling of atomization processes. PhD Thesis, Purdue University; 1996.
- [33] Smirnov VI. *A course of higher mathematics*. New York: Pergamon Press; 1964.
- [34] Kreyszig E. *Advanced engineering mathematics*. New York: Wiley; 1993. p. 949–56.
- [35] Longuet-Higgins MS, Cokelet ED. The deformation of steep surface waves on water. *Proc R Soc Lond A* 1976;350:1–26.
- [36] Spyropoulos ET, Blaisdell GA. Evaluation of the dynamic model for simulations of compressible decaying isotropic turbulence. *AIAA J* 1996;34(5):990–8.
- [37] Hilbing JH, Heister SD, Spangler CA. A boundary-element method for atomization of a finite liquid jet. *Atomization Sprays* 1995;5: 621–38.
- [38] Lele SK. Compact finite difference schemes with spectral-like resolution. *J Computat Phys* 1992;103:16–42.
- [39] Proakis JG, Manolakis DG. *Digital signal processing*. New Jersey: Prentice-Hall; 1996. pp. 30–1.
- [40] White FM. *Viscous fluid flow*, 2nd ed. New York: McGraw Hill; 1991. p. 235, 269, 358.
- [41] Thwaites B. *Incompressible aerodynamics*. New York: Dover; 1960. p. 30–1.
- [42] Brennen C. Cavity surface wave patterns and general appearance. *J Fluid Mech* 1970;44(1):33–49.
- [43] Shames IH. *Engineering mechanics*. New Jersey: Prentice-Hall; 1993. p. 306–8.
- [44] Rupe JH. On the dynamic characteristics of free liquid jets and a partial correlation with orifice geometry. NASA JPL Tech Rep 1962; 32–207.
- [45] Sterling AM, Sleicher CA. The instability of capillary jets. *J Fluid Mech* 1975;68(3):477–95.
- [46] Hoyt JW, Taylor JJ. Waves on water jets. *J Fluid Mech* 1977;83: 119–27.
- [47] Widnall SE, Sullivan JP. On the stability of vortex rings. *Proc R Soc Lond, Ser A* 1973;332(1590):335–53.
- [48] Kerswell RR. Elliptical instability. *Ann Rev Fluid Mech* 2002;34: 83–113.
- [49] Bayly BJ. Three-dimensional instability of elliptical flow. *Phys Rev Lett* 1986;34:2160–3.
- [50] Waleffe F. On the three-dimensional instability of strained vortices. *Phys Fluids, A* 1990;2(1):76–80.
- [51] Landman MJ, Saffman PG. The three-dimensional instability of strained vortices in a viscous fluid. *Phys Fluids* 1987;30(8): 2339–42.
- [52] Wu PK, Tseng LK, Faeth GM. Primary breakup in gas/liquid mixing layers for turbulent liquids. *Atomization Sprays* 1992;2: 295–317.
- [53] Hoyt JW, Taylor JJ. Effect of nozzle boundary layer on water jets discharging in air. In *Jets and Cavities—International Symposium, ASME*, held in Miami Beach, Florida, November 17–22; 1985. p. 93–100.
- [54] Rayleigh WS. On the instability of jets. *Proc London Math Soc* 1878; 10(4).
- [55] Yuen MC. Non-linear capillary instability of a liquid jet. *J Fluid Mech* 1968;33(1):151–63.
- [56] Goedde EF, Yuen MC. Experiments on liquid jet instability. *J Fluid Mech* 1970;40(3):495–514.
- [57] McCarthy MJ, Molloy NA. Review of stability of liquid jets and the influence of nozzle design. *Chem Engng J* 1974;7:1–20.